J Solid State Electrochem (2005) 9: 547–557
DOI 10.1007/s10008-004-0590-1

ORIGINAL PAPER

Ekaterina V. Tsipis · Vladislav V. Kharton
Jorge R. Frade · Pedro Núñez

High-temperature transport and electrochemical properties of $YBaCo_4O_{7+\delta}$

Received: 30 June 2004 / Accepted: 27 September 2004 / Published online: 23 December 2004

Abstract The total conductivity of oxygen-hyperstoichiometric $YBaCo_4O_{7+\delta}$ is predominantly p-type electronic at oxygen partial pressures from 5×10^4 Pa down to the phase decomposition limit, 10^{-11}–10^{-4} Pa at 973–1223 K. The ion transference numbers, determined by the oxygen permeation and faradaic efficiency measurements at 1073–1223 K, vary in the range 3×10^{-5}–2×10^{-4} and increase with temperature. The oxygen permeability of $YBaCo_4O_{7+\delta}$ ceramics, with overall level similar to that of K_2NiF_4-type cuprates, is mainly limited by the bulk ionic conduction. Heating above 1050–1100 K and redox processes under oxidizing conditions lead to a first-order transition accompanied with extensive oxygen losses from the lattice, resulting in decreasing total oxygen content from 8.5 down to approximately seven atoms per unit formula. Except for the variations associated with this transition, the electron–hole conductivity and Seebeck coefficient are essentially $p(O_2)$-independent within the phase stability limits. The use of different synthesis methods, namely the standard ceramic technique and the glycine–nitrate process, has no significant effect on the properties of $YBaCo_4O_{7+\delta}$ ceramics. The thermal expansion coefficients averaged at 600–1100 K in air are $(7.3–7.6)\times10^{-6}$ K^{-1}. Porous $YBaCo_4O_7$-based cathodes show a very high electrochemical activity in contact with $LaGaO_3$-based solid electrolyte at 873–1073 K.

E. V. Tsipis · V. V. Kharton · J. R. Frade
Department of Ceramics and Glass Engineering, CICECO, University of Aveiro, 3810-193 Aveiro, Portugal

V. V. Kharton (✉)
Institute of Physicochemical Problems, Belarus State University, 14 Leningradskaya Str., 220050 Minsk, Belarus
E-mail: kharton@cv.ua.pt
Tel.: +351-234-370263
Fax: +351-234-425300

P. Núñez
Department of Inorganic Chemistry, University of La Laguna, 38200 La Laguna, Tenerife, Spain

Keywords Yttrium–barium cobaltite · Solid oxide fuel cell cathode · Electron–hole conductivity · Oxygen ionic transport · Transference number

Introduction

Perovskite-related cobaltites possess very high levels of mixed ionic–electronic conductivity and catalytic activity, making them attractive for numerous high-temperature electrochemical applications, including electrodes of solid oxide fuel cells (SOFCs) and dense ceramic membranes for oxygen separation and partial oxidation of light hydrocarbons [1–3]. Practical use of Co-containing membranes is, however, limited owing to their poor stability in reducing atmospheres and high chemical-induced expansion under varying oxygen partial pressure [1–5]. Although these problems could be partly solved by applying a mixed-conducting protective layer on the membrane surface, the use of protective layers is hampered by excessively high thermal expansion coefficients (TECs) of cobaltite phases, associated with extensive oxygen nonstoichiometry variations and numerous transitions in the electronic sublattice when temperature increases [1, 3–6]. The former contribution to TECs results from a continuous increase in the average size of Co cations due to oxygen losses on heating, and is characteristic of perovskite-type cobaltites containing Co^{4+}, such as $La(Sr)CoO_{3-\delta}$. Analogously, cobaltite cathode layers exhibit a superior electrochemical performance with respect to common electrode materials based on $La(Sr)MnO_3$ [3, 6, 7]. This may be of great interest for intermediate-temperature SOFCs operating at 773–1073 K, the performance of which is limited by the electrode polarization. However, high TECs of perovskite-like cobaltites are incompatible with those of solid electrolyte materials such as doped lanthanum gallate, ceria or stabilized zirconia [3, 6]. For various intergrowth structures stabilizing Co^{2+} and Co^{3+} cations, thermal expansion is, as a rule,

considerably lower compared with that of the perovskites [3, 8]. At the same time, information on ionic and electronic transport in layered cobaltites is scarce, and is insufficient to evaluate these materials for potential use in electrochemical devices.

One interesting example of intergrowth cobaltite compounds is $YBaCo_4O_7$, recently characterized from the structural point of view and reported to contain divalent and trivalent cobalt only [9]. This crystal structure (Fig. 1), firstly reported for $HoBaCo_4O_7$ [10] and similar to the structures of hexagonal $Ba_2Er_2Zn_8O_{13}$ [11] and $BaIn_2Zn_3O_7$ [12] comprises two distinct cobalt sites, Co1 and Co2, both tetrahedrally coordinated. The Co1-to-Co2 concentration ratio is 3:1; the space group was reported as $P6_3mc$ [9, 10]. The large Ba^{2+} cations occupy cavities between alternating layers of $(Co1)O_4$ tetrahedra and layers composed by $(Co2)O_4$ and octahedrally coordinated Y^{3+}. Although no information on the high-temperature transport properties of $HoBaCo_4O_7$ and $YBaCo_4O_7$ is available yet, the data on other compositions of Y–Ba–Co–O system [13] enable us to expect a significant level of oxygen ionic conduction. For instance, dense membranes of multiphase $Y_{0.05}BaCo_{0.95}O_{3-\delta}$ ceramics exhibit oxygen permeation fluxes as high as 3.9×10^{-7} mol cm^{-2} s^{-1} at 1173 K [13].

As a continuation of our research of mixed-conducting cobaltites [14–17], the present work is focused on the characterization of physicochemical and electrochemical properties of $YBaCo_4O_7$ at elevated temperatures. Particular emphasis is given to the properties important for practical applications, including partial electronic and ionic conductivities, oxygen permeability, thermal expansion, phase stability and cathode performance. The cathode overpotentials were measured in order to assess the electrocatalytic activity of $YBaCo_4O_7$ as a potential electrode material rather than to determine cathode reaction mechanisms, which will be considered in a separate publication. Therefore, the data on electrochemical behavior, presented in this work, are limited to the overpotential–current dependencies of porous $YBaCo_4O_7$ layers. These electrodes, both pure and with moderate additions of metallic silver as a sintering aid and a promoter of oxygen exchange [18], were studied in contact with a $(La_{0.9}Sr_{0.1})_{0.98}Ga_{0.8}Mg_{0.2}O_{3-\delta}$ (LSGM) solid electrolyte characterized earlier [19]. In order to identify possible microstructural effects on the transport properties, $YBaCo_4O_7$ samples were prepared using two different synthesis methods, namely the standard ceramic technique and the glycine–nitrate process (GNP). The latter, a self-combustion method using glycine as a fuel and chelating agent and nitrates of the metal components as oxidants, is well known to be especially appropriate for multicomponent perovskite systems and to provide a large specific surface area important for porous electrode layers [20].

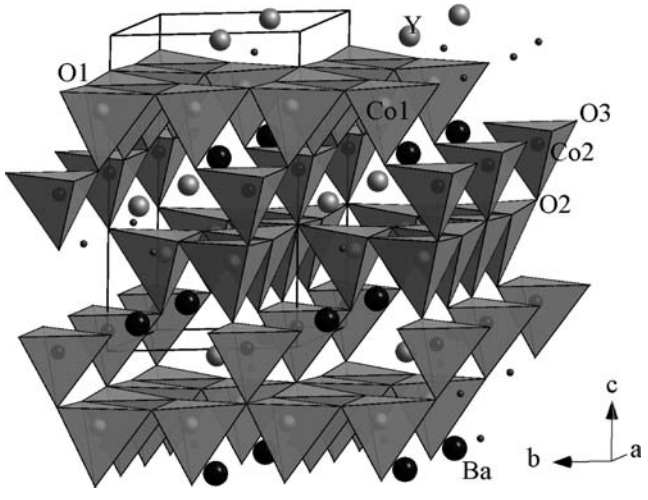

Fig. 1 Crystal structure of $YBaCo_4O_7$ according to the model from Ref. [9]. *Solid lines* show one hexagonal unit cell

Experimental

The standard ceramic route, hereafter referred to as method 1, included mixing of stoichiometric amounts of high-purity Y_2O_3, $BaCO_3$ and $Co(NO_3)_2{\cdot}6H_2O$, annealing at 1073 K for 5 h, ball-milling, and final reaction at 1273 K for 5 h in air. For the GNP (method 2), $BaCO_3$ was dissolved in an aqueous solution of nitric acid, with subsequent dissolution of stoichiometric amounts of $Y(NO_3)_3{\cdot}6H_2O$ and $Co(NO_3)_2{\cdot}6H_2O$. The glycine was added to this solution in a double amount to the stoichiometry, assuming H_2O, CO_2 and N_2 to be the only gaseous reaction products; thus, the molar glycine-to-nitrate ratio was 10:9. Then the solution was evaporated on a hot plate until a self-sustaining reaction occurred; the resultant powder was annealed at 1073 K for 2 h and ball-milled. Dense ceramic samples were uniaxially pressed (200–250 MPa) into discs of 18-mm diameter and were then sintered in air for 2 h; for the materials synthesized by methods 1 and 2, the sintering temperature was 1523 and 1473 K, respectively. After sintering, the samples were slowly cooled (1–2 K min^{-1}) and were kept in dry CO_2-free air for 10–20 days in order to achieve an equilibrium oxygen content at low temperatures. The density of the ceramics, determined by the standard pycnometric technique, was 93–98% of the theoretical value(Table 1).

Materials characterization included X-ray diffraction (XRD), emission spectroscopic analysis, scanning electron microscopy (SEM) coupled with energy-dispersive spectroscopy (EDS), thermogravimetric analysis (TGA) and differential thermal analysis (DTA), dilatometry, and measurements of total conductivity (four-probe direct current) and the Seebeck coefficient as functions of oxygen partial pressure. The experimental procedures and equipment used for the characterization were described elsewhere [14–19, 21]. The XRD spectra were recorded at room temperature using a Rigaku D/Max-B diffractometer (Cu Kα radiation, 2θ range from 10 to 120°, step 0.02°, 7 s per step). Structure refinement was

Table 1 Properties of $YBaCo_4O_{7+\delta}$ ceramics prepared by methods 1 and 2

Synthesis technique	Unit cell parameters		Relative density (%)	Average linear thermal expansion coefficient in air		Activation energy for total conductivity in air	
	a (nm)	c (nm)		T (K)	$\bar{\alpha} \times 10^6$ (K^{-1})	T (K)	E_a (kJ mol^{-1})
Method 1	0.6302(2)	1.0243(9)	97.5	420–660	9.00 ± 0.09	620–1070	21.7 ± 0.2
				750–1270	7.61 ± 0.02	1090–1250	22.5 ± 0.4
Method 2	0.6303(5)	1.0248(3)	92.9	470–760	7.29 ± 0.04	270–770	20 ± 2
				800–1220	7.27 ± 0.05	1080–1250	21 ± 4

performed using the Fullprof program [22] and the space group $P6_3mc$ [9, 10]; the structural data [9] obtained by neutron diffraction were used as a starting model. For the TGA/DTA studies, $YBaCo_4O_7$ powders prepared by grinding of dense ceramics were preannealed at 1273 K in flowing air purified from water vapor and CO_2, with subsequent slow (1–2 K min^{-1}) cooling in the same flow. The oxygen ionic transport parameters were calculated from the data on steady-state oxygen permeation and faradaic efficiency, as described elsewhere [15, 19]. The electrode polarization measurements were carried out by the three-electrode technique in cells with porous Pt counter and reference electrodes [14, 23]. The $YBaCo_4O_7$ electrode layers were made from the GNP-synthesized powder. According to previous results [18], highly dispersed metallic silver (10 wt%) was added into the paste used for fabrication of some electrodes. Pure and Ag-containing layers (sheet density of 15 ± 5 mg cm^{-2}) were screen-printed onto LSGM ceramics [19] and then sintered in air for 2 h at 1343 and 1273 K, respectively. The reproducibility of the electrochemical data was verified by studying two to three similar electrodes prepared under identical conditions; one example is shown in the inset of Fig. 2. The phase composition and the microstructure of the electrode layers before and after electrochemical measurements were studied by XRD and SEM/EDS.

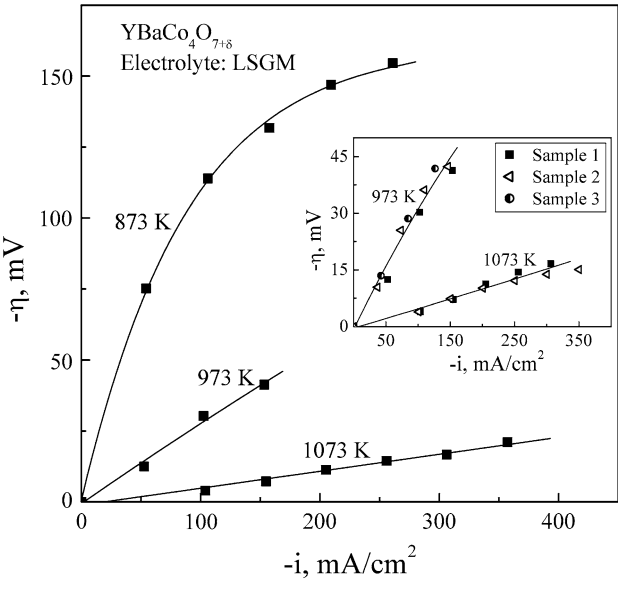

Fig. 2 Current dependencies of the cathodic overpotential of a $YBaCo_4O_{7+\delta}$ layer in contact with $(La_{0.9}Sr_{0.1})_{0.98}Ga_{0.8}Mg_{0.2}O_{3-\delta}$ (*LSGM*) solid electrolyte. The *inset* shows the reproducibility of the data, measured for three different cells

Results and discussion

General characterization

The XRD analysis of $YBaCo_4O_7$ powders and ceramics, prepared by both methods, showed apparent adequacy of the structural model proposed in Ref. [9]. No phase impurities were found; the unit cell parameters are very similar for both synthesis methods (Table 1). SEM/EDS analysis confirmed the absence of substantial grain-boundary anomalies. Figure 3a and b compares typical SEM micrographs of fractured ceramics prepared by methods 1 and 2. The grain size varies in the range 2–10 μm, being slightly larger for the material synthesized via method 1 owing to the higher sintering temperature.

In contrast to the structural model [9], however, the TGA results obtained under reduction in a flowing 5% H_2–95% Ar mixture showed that the oxygen content in the title material is considerably higher than seven atoms per unit formula (Fig. 4, inset). At room temperature, the total oxygen content is 8.58, which corresponds to an average cobalt oxidation state of +3.04. This contradicts the assumption [9] that $YBaCo_4O_7$ is nearly stoichiometric or even slightly oxygen deficient at 300 K. On heating in air, extensive weight losses are observed at 1110–1200 K, which cannot be attributed to $BaCO_3$ decomposition on the surface, characteristic of Ba-containing oxide materials [9, 26, 27], as the powder was annealed in flowing CO_2-free air prior to the measurements. Therefore, these weight changes are associated with oxygen losses from the lattice, leading to the formation of nearly oxygen stoichiometric $YBaCo_4O_{7+\delta}$ at temperatures above 1200 K (Fig. 4). Note that even at $T > 1200$ K this phase still contains a small amount of hyperstoichiometric oxygen, $\delta \approx 0.14$. The oxygen losses on heating are accompanied by two endothermic effects at approximately 1135 and 1170 K.

The dilatometric curves of $YBaCo_4O_7$ ceramics, measured with a heating rate of 5 K min^{-1}, were found to be almost linear (Fig. 5). At temperatures above 750 K, the average TECs of materials prepared by the two different methods are quite close, (7.3–7.6)×10^{-6} K^{-1} (Table 1). In the low-temperature range,

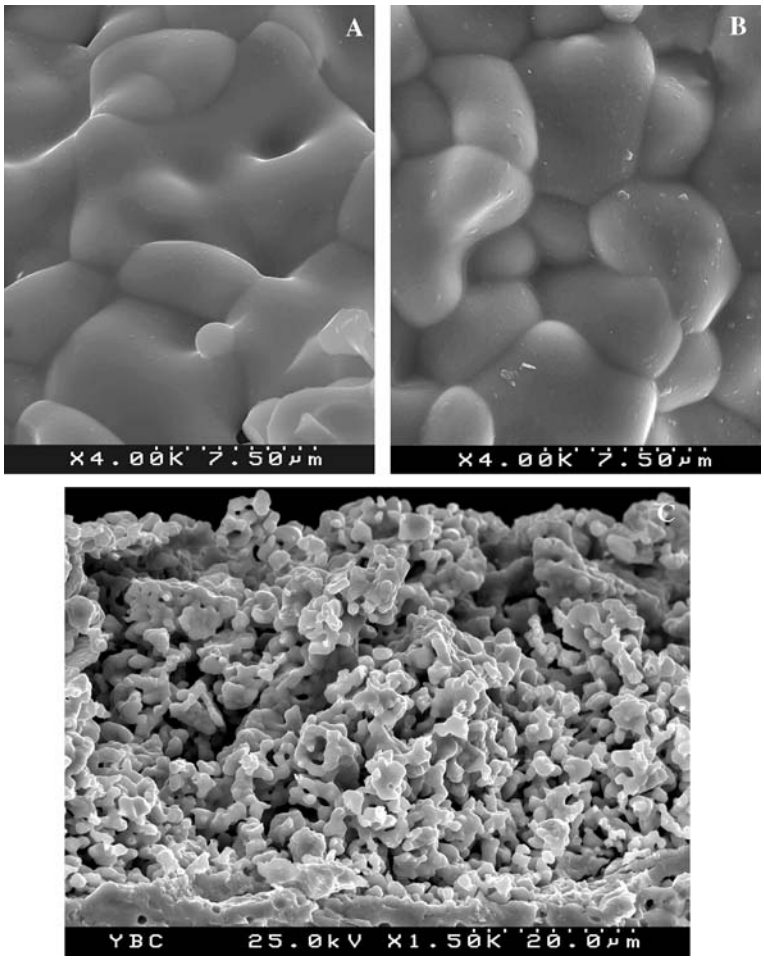

Fig. 3 Scanning electron microscopy (*SEM*) micrographs of fractured $YBaCo_4O_{7+\delta}$ ceramics prepared via method 1 (**a**) and method 2 (**b**), and the $YBaCo_4O_{7+\delta}$ cathode (**c**)

the difference in the TECs is slightly higher, probably owing to an experimental error that might result, in particular, from the hysteresis phenomena discussed later. Although the apparent linearity of the dilatometric curves might indicate the absence of phase transitions, the isothermal dilatometric measurements showed a significant volume contraction at temperatures around 1173–1223 K as illustrated in the inset of Fig. 5; the average TEC on further cooling was close to that on heating. No indication of the contraction phenomena was observed at temperatures below 1100 K. Shrinkage of the ceramics due to additional sintering is very unlikely since 93–97% density was already achieved in the course of sintering at 1473–1523 K. Respectively, the TGA/DTA and dilatometry results are considered as indicative of first-order phase transition(s) at 1173–1223 K, accompanied by or induced by kinetically stagnated oxygen stoichiometry variations. These kinetic limitations should be much more pronounced in the case of experiments using dense ceramics, such as dilatometry or total conductivity measurements, in comparison with TGA/DTA, where powdered samples are tested. As a particular result, no phase changes are visible in the course of standard dilatometric measurements on heating with a fixed rate (Fig. 5).

A similar conclusion was drawn considering the data on total conductivity (Fig. 6). Heating up to 1040–1070 K leads to a drastic increase of the conductivity (σ); then, at 1190–1215 K, the values of σ decrease back to the initial level. Except for a reasonable hysteresis shift, this anomaly is well reproducible on cooling. The activation energies before and after phase transition are equal within the limits of experimental error (Table 1). At temperatures close to the conductivity maximum, the equilibration kinetics was very slow; the time necessary to achieve time-independent σ values after a temperature change was as long as 50–250 h. For comparison, when the temperature was significantly lower or higher, the relaxation time was no longer than 0.5–2.0 h. As for the lattice parameters and thermal expansion, the effect of the synthesis route on the total conductivity was found to be negligible (Fig. 6).

In order to reveal possible structural changes, a series of $YBaCo_4O_{7+\delta}$ samples were annealed in air at temperatures from 1173 to 1523 K with subsequent quenching in liquid nitrogen and XRD analysis. However, these attempts failed owing to insufficient sensitivity of XRD to the oxygen site occupancy. In fact, the XRD patterns of $YBaCo_4O_{7+\delta}$, quenched from high temperatures and equilibrated at room temperature, are

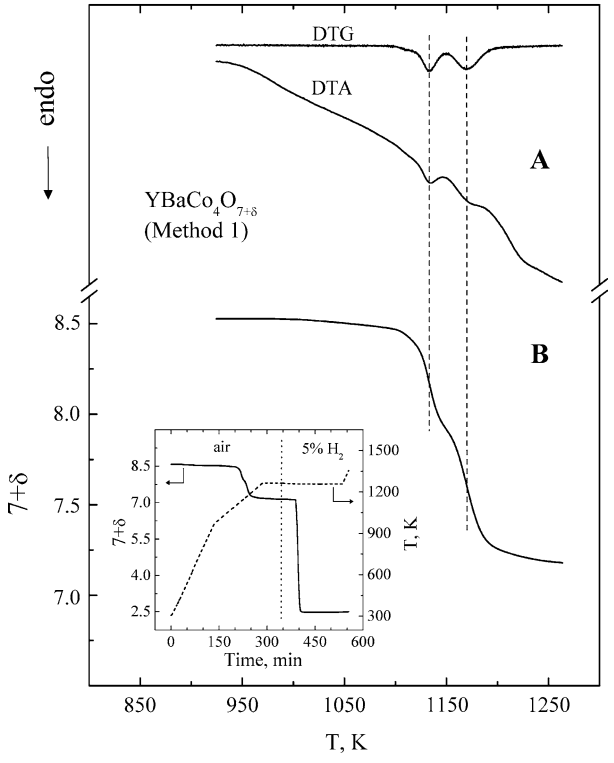

Fig. 4 Diffrential thermogravimetry (*DTG*) and differential thermal analysis (*DTA*) curves (*a*) and variations of oxygen content (*b*) of $YBaCo_4O_{7+\delta}$ powder obtained by grinding of ceramic samples, synthesized by method 1 (see text). The *inset* shows the oxygen content variations under reduction in a 5% H_2–95% Ar flow

similar to each other (Fig. 7). Therefore, detailed calorimetric and neutron diffraction studies are necessary to identify the exact nature of the observed phase transformation(s); these investigations are now in progress. One should separately note that at the elevated temperatures studied in this work, any long-range charge ordering phenomena are very unlikely. For instance, charge ordering in the cobalt sublattice of $LnBaCo_2O_5$ (Ln is Y, Tb, Dy, Ho) is observed only below about 210 K [24, 25].

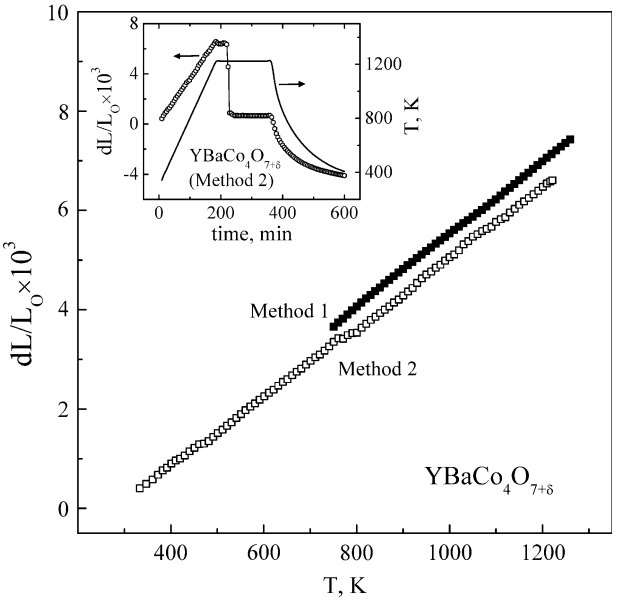

Fig. 5 Dilatometric curves of $YBaCo_4O_{7+\delta}$ ceramics, prepared using methods 1 and 2, on heating in air. The *inset* shows the relative elongation in the course of heating, isothermal annealing at 1223 K, and subsequent cooling

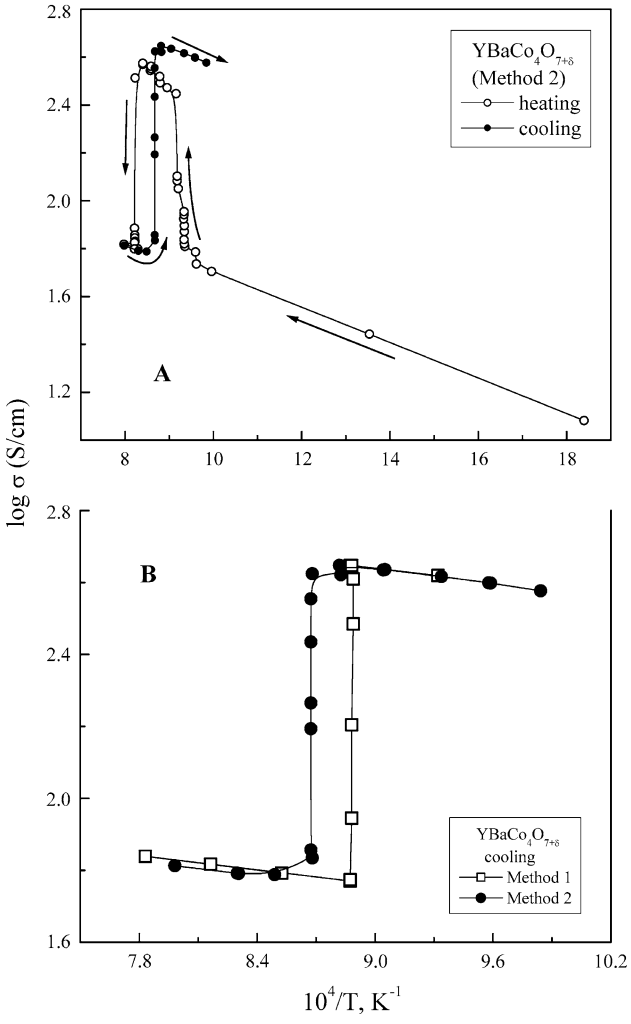

Fig. 6 Temperature dependence of the total conductivity of $YBaCo_4O_{7+\delta}$ ceramics in air

Electrical properties versus oxygen partial pressure

Representative examples of the $p(O_2)$-dependencies of the total conductivity and the Seebeck coefficient (α) are shown in Figs. 8 and 9. The electrical properties of $YBaCo_4O_{7+\delta}$ ceramics at 973–1023 K are essentially independent of the oxygen partial pressure until phase decomposition; the phase stability boundaries confirmed by XRD (Fig. 7) are marked in Fig. 9 by dashed lines. This type of behavior is typical for oxide phases where the oxygen stoichiometry variations with oxygen pressure are very low [28, 29]. Within all the $p(O_2)$ range studied, the Seebeck coefficient was found to be positive.

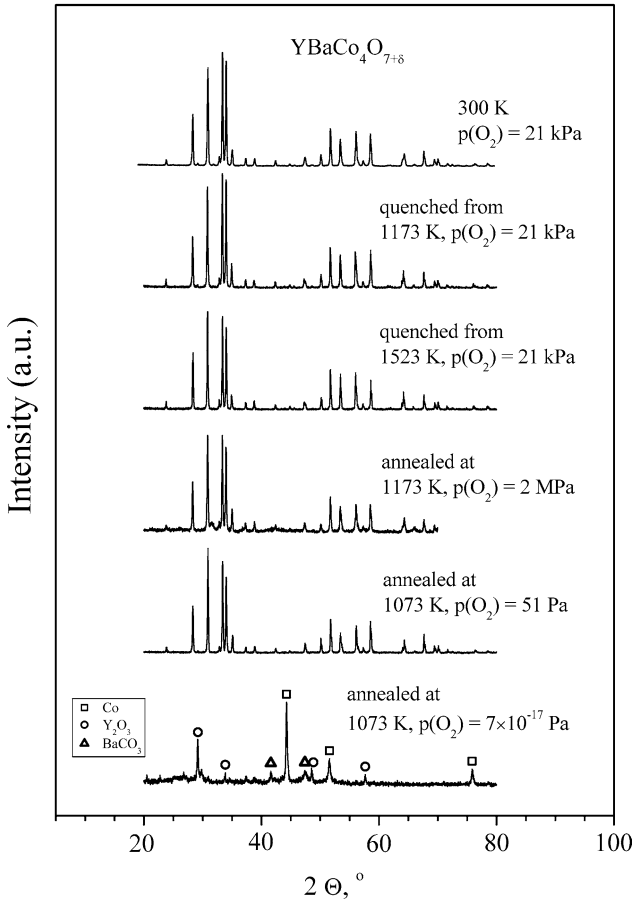

Fig. 7 X-ray diffraction patterns of $YBaCo_4O_{7+\delta}$ after treatment in various atmospheres

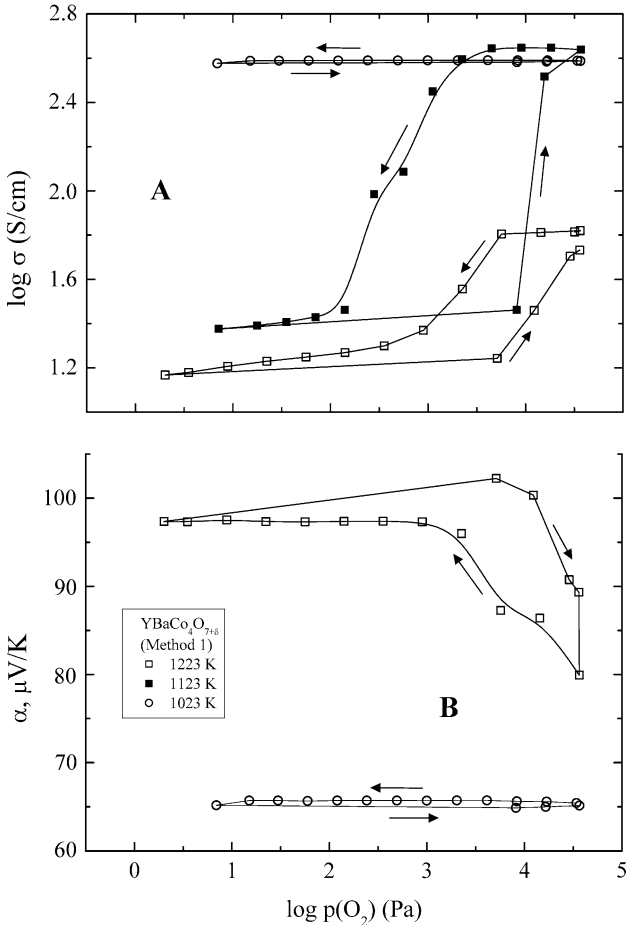

Fig. 8 Oxygen partial pressure dependencies of the total conductivity (**a**) and the Seebeck coefficient (**b**) of $YBaCo_4O_{7+\delta}$ under oxidizing conditions. *Arrows* show the direction of $p(O_2)$ changes

As the oxygen ion transference numbers (t_o) of $YBaCo_4O_{7+\delta}$ are lower than 10^{-3} (Table 2), the sign of the thermopower unambiguously indicates that the conductivity is predominantly p-type electronic.

At 1073–1223 K, an oxygen-pressure-dependent phase transition is observed (Fig. 8). Reducing $p(O_2)$ from 5×10^4 down to 10 Pa leads to a lower total conductivity and higher thermopower, both showing large hysteresis phenomena. As expected for a p-type semiconductor [1, 7, 28], the decrease in the conductivity is associated with oxygen losses from the lattice. Upon further reduction, the electrical properties become essentially $p(O_2)$-independent (Fig. 9). The transition observed on reduction occurs in the same temperature range as phase changes in air (Fig. 6) and has evidently the same nature. Again, however, no essential differences detectable by XRD are observed for $YBaCo_4O_{7+\delta}$ samples annealed at $p(O_2) = 51$ Pa and 2 MPa, i.e., at oxygen chemical potentials far from atmospheric (Fig. 7). As a possible hypothesis, the observed behavior can be explained by oxygen intercalation into the layer built of the $(Co1)O_4$ tetrahedra. Since these cations form a continuous 2D network of Co–O bonds, increasing the hole concentration in the $(Co1)O_4$ layer might have a drastic effect on the conductivity as observed experimentally; heating or reducing $p(O_2)$ would decrease the total oxygen content and, thus, the concentration of mobile p-type charge carriers.

In spite of the hole transport mechanism, one should mention that the total conductivity of the $YBaCo_4O_{7+\delta}$ phase, 30–65 S cm^{-1} at 773–1073 K, is sufficient for the use in SOFC cathodes. The $p(O_2)$-independent conductivity values suggest that high cathodic polarization should have no effect on the electrical properties of electrode layers. However, the volume variations at temperatures above 1100 K may lead to mechanical stresses and incompatibility with solid electrolyte materials, thus enabling application of $YBaCo_4O_{7+\delta}$ cathodes only in the intermediate temperature range.

Phase stability

Decreasing oxygen partial pressures below approximately 2×10^{-11} Pa at 973 K and 3×10^{-4} Pa at 1173 K results in a decomposition of the $YBaCo_4O_{7+\delta}$ phase, accompanied by irreversible degradation of the electrical properties and poor reproducibility of results. Figure 10

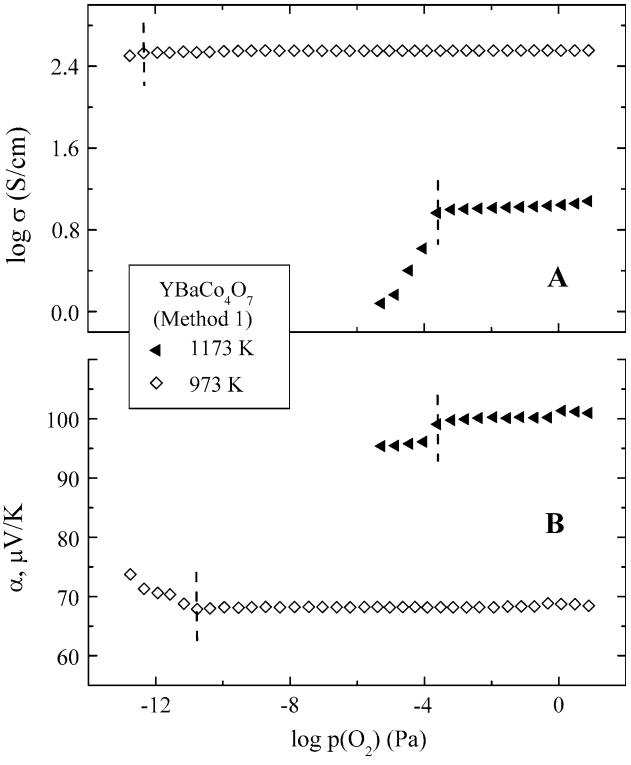

Fig. 9 Oxygen partial pressure dependencies of the total conductivity (**a**) and the Seebeck coefficient (**b**) of $YBaCo_4O_{7+\delta}$, prepared by method 1, under moderately oxidizing and reducing conditions. *Dashed lines* indicate the phase stability limit

compares the stability boundary of $YBaCo_4O_{7+\delta}$, estimated from the $p(O_2)$ dependencies of the Seebeck coefficient as shown in Fig. 9, with literature data on cobalt oxide [30] and perovskite-type lanthanum cobaltite [31]. The decomposition of yttrium–barium cobaltite occurs at oxygen partial pressures 10^2–10^4 times higher than that for CoO, but considerably lower with respect to $LaCoO_{3-\delta}$, where the basic oxidation state of the cobalt cations is +3. This suggests that $YBaCo_4O_{7+\delta}$ decomposes into a mixture of binary metal oxides when most Co^{3+} cations are converted into Co^{2+}; further reduction leads to the formation of metallic cobalt (Fig. 7). Such behavior may indicate that the model [9], which postulates the presence of 75% Co^{2+} and 25% Co^{3+} in the structure of $YBaCo_4O_7$, may be valid at moderate $p(O_2)$ when all extra oxygen left the lattice.

Oxygen ionic transport

The results of faradaic efficiency studies, performed under zero oxygen chemical potential in air [19], show that the oxygen ionic contribution to the total conductivity of $YBaCo_4O_{7+\delta}$ at 1173–1223 K is lower than 0.01% (Table 2). Therefore, for a $YBaCo_4O_{7+\delta}$ membrane placed under an oxygen chemical potential gradient, the ambipolar conductivity determining oxygen transport through the membrane bulk is governed by the ionic conduction; the effect of p-type electronic conductivity is expected to be negligible. In order to identify if the overall oxygen transport is influenced by surface-exchange kinetics in addition to bulk diffusion, the oxygen permeation fluxes (j) were measured as a function of the membrane thickness (Fig. 11a). The specific oxygen permeability $J(O_2)$, shown in Fig. 11b, was calculated as [14–17]

$$j = \frac{J(O_2)}{d} \ln\left(\frac{p_2}{p_1}\right), \quad (1)$$

where d is the membrane thickness, and p_1 and p_2 are the oxygen partial pressures at the membrane permeate and feed sides, respectively. The permeability, proportional to jd by definition, should be thickness-independent if the permeation is determined by the bulk ionic conduction, i.e., the integral form of the Wagner law is observed. In this case, the specific oxygen permeability is proportional to the ionic conductivity (σ_o) averaged in a given oxygen chemical potential gradient:

$$J(O_2) = \frac{RT}{16F^2}\bar{\sigma}_o. \quad (2)$$

In contrast, if the surface limitations to overall oxygen transport are considerable, $J(O_2)$ should increase with membrane thickness as the role of the surface exchange decreases.

The data on $YBaCo_4O_{7+\delta}$ ceramics (Fig. 11) suggest the presence of minor surface limitations to the permeation flux, the role of which increases with decreasing

Table 2 Oxygen ion transference numbers of $YBaCo_4O_{7+\delta}$ ceramics prepared by methods 1 and 2. The faradaic efficiency (*FE*) measurements were performed under zero oxygen chemical potential gradient in air. The transference numbers calculated from the oxygen permeation (*OP*) data are averaged in the p_1 range from 5 to 10 kPa, at fixed $p_2 = 21$ kPa. d is the membrane thickness

T (K)	Method 1 (OP, $d = 0.60$ mm)	Method 2		
		OP		FE
		$d = 0.60$ mm	$d = 1.00$ mm	$d = 1.00$ mm
1223	1.8×10^{-4}	1.5×10^{-4}	1.8×10^{-4}	9.1×10^{-5}
1173	1.7×10^{-4}	1.4×10^{-4}	1.5×10^{-4}	7.2×10^{-5}
1123	1.2×10^{-4}	1.1×10^{-4}	1.2×10^{-4}	
1073	2.9×10^{-5}		3.9×10^{-5}	

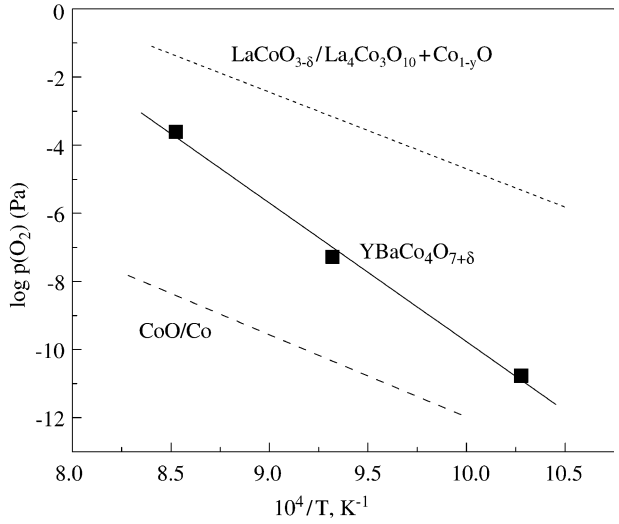

Fig. 10 Low-$p(O_2)$ stability boundary of the $YBaCo_4O_{7+\delta}$ phase, evaluated from the data on the Seebeck coefficient versus oxygen pressure. Literature data on CoO [30] and $LaCoO_{3-\delta}$ [31] are shown for comparison

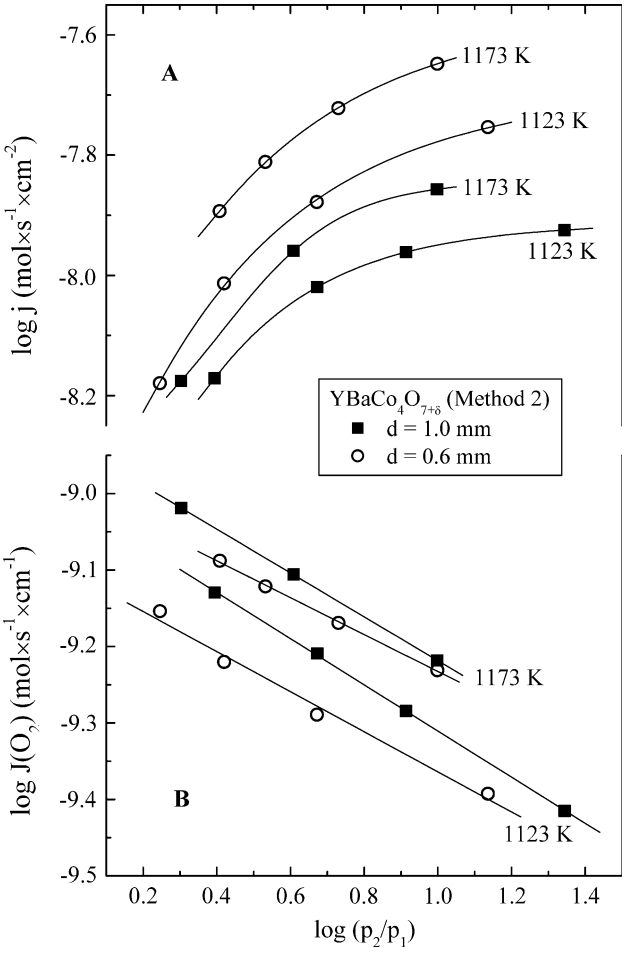

Fig. 11 Dependence of the oxygen permeation fluxes (**a**) and specific oxygen permeability (**b**) of $YBaCo_4O_{7+\delta}$ membranes, prepared using method 2, on the oxygen partial pressure gradient

temperature. However, the difference in the $J(O_2)$ values of membranes with different thickness is comparable to experimental error. The values of the oxygen ionic conductivity and the transference numbers, calculated from the permeation data using Eq. (2), are similar within the limits of experimental uncertainty (Tables 2, 3). Moreover, these values are in reasonable agreement with those measured by the faradaic efficiency method if one takes into account that, owing to a higher permeate-side oxygen pressure in the latter case, the ion transference numbers determined by the faradaic efficiency technique should be lower than those calculated from the oxygen permeation data (Fig. 8). One may therefore conclude that the surface-exchange effects on the oxygen permeation through $YBaCo_4O_{7+\delta}$ ceramics at 1073–1223 K can be neglected. Another necessary comment is that, as for other properties, the ionic conductivity and oxygen permeability of $YBaCo_4O_{7+\delta}$ are independent of the synthesis method.

Figure 12 compares the level of oxygen permeation fluxes through $YBaCo_4O_{7+\delta}$ ceramics and several Co-containing perovskites [17, 32–34]. In order to provide a comparison of membranes with different thickness, the permeation fluxes are expressed as *jd*. The permeability of oxygen-deficient materials based on $SrCoO_{3-\delta}$ is 30–150 times higher than that of $YBaCo_4O_{7+\delta}$. At the same time, the ionic transport in undoped $SrCoO_{3-\delta}$ at 973–1100 K shows a negligible dependence on temperature, as for $YBaCo_4O_{7+\delta}$ at 1123–1223 K. In both cases this behavior is ascribed to temperature-induced phase transitions. Strontium cobaltite with cubic perovskite structure is stable under oxidizing conditions at temperatures above 1120–1220 K and undergoes a series of phase transformations on cooling; depending on moderate $p(O_2)$ variations a number of phases, such as brownmillerite-type $Sr_2Co_2O_{5+\delta}$ and rhombohedral $Sr_6Co_5O_{15}$, may be formed [34–36]. Cubic perovkite $SrCo_{0.95}Cr_{0.05}O_{3-\delta}$ decomposes into a phase mixture on cooling to temperatures below 1000 K, resulting in a drastic drop of the apparent activation energy for oxygen permeation. Similar behavior is characteristic for most $SrCoO_3$-based ceramics where the concentration of dopants is insufficient to stabilize the cubic perovskite lattice [33, 34].

With respect to perovskite $La_{0.8}Sr_{0.2}Fe_{0.8}Co_{0.2}O_{3-\delta}$, which belongs to another series of materials promising for SOFCs and oxygen membranes [32, 37],

Table 3 Oxygen ionic conductivity of $YBaCo_4O_{7+\delta}$ (mS cm^{-1}) evaluated from the data on oxygen permeation and total conductivity

T (K)	Method 1	Method 2	
	d = 0.60 mm	*d* = 0.60 mm	*d* = 1.00 mm
1223	11.6	9.7	11.3
1173	10.4	8.5	9.4
1123	6.7	6.4	7.0
1073	1.6	–	2.1

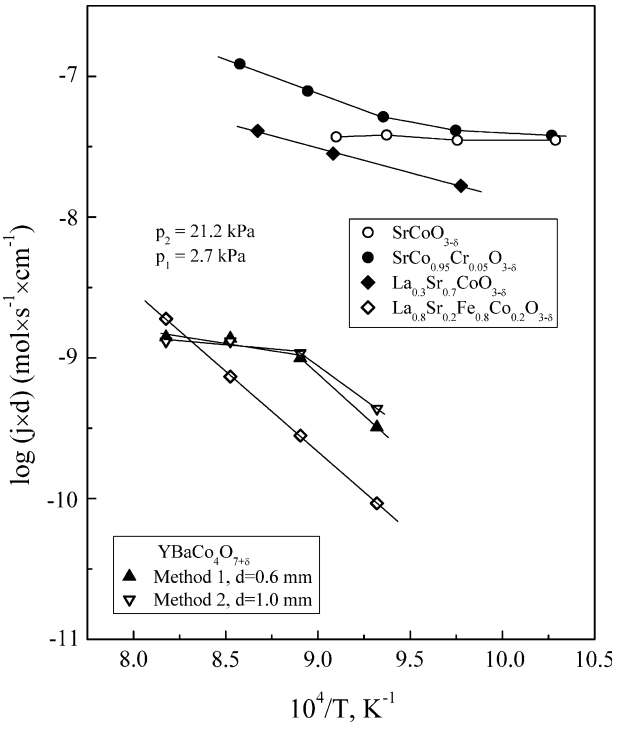

Fig. 12 Temperature dependence of the oxygen permeation fluxes through $YBaCo_4O_{7+\delta}$ ceramics, normalized to the membrane thickness, under a fixed oxygen partial pressure gradient. Previous data [17, 32–34] on $SrCoO_{3-\delta}$ ($d = 1.20$ mm), $SrCo_{0.95}Cr_{0.05}O_{3-\delta}$ ($d = 2.10$ mm), $La_{0.3}Sr_{0.7}CoO_{3-\delta}$ ($d = 1.00$ mm) and $La_{0.8}Sr_{0.2}Fe_{0.8}Co_{0.2}O_{3-\delta}$ ($d = 1.00$ mm) are shown for comparison

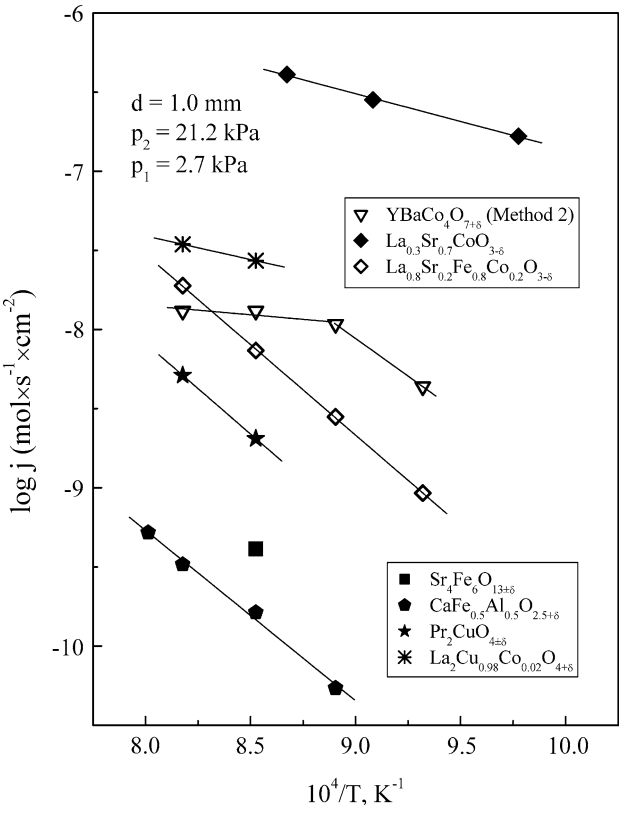

Fig. 13 Comparison of the oxygen permeation fluxes through various mixed-conducting materials [17, 32, 38–40]

$YBaCo_4O_{7+\delta}$ exhibits a considerably higher oxygen permeation at 1073–1173 K (Fig. 12). This level of oxygen transport is also greater than that in layered Fe-containing phases such as $Sr_4Fe_6O_{13\pm\delta}$ [38] or $CaFe_{0.5}Al_{0.5}O_{2.5+\delta}$ [39], but is rather moderate if compared with that in K_2NiF_4-type cuprates [40]. Figure 13 presents an overview on the oxygen permeability of various intergrowth materials.

Electrochemical activity of $YBaCo_4O_{7+\delta}$ electrodes

The use of GNP-synthesized $YBaCo_4O_{7+\delta}$ powder makes it possible to fabricate porous cathode layers with well-developed microstructure (Fig. 3c), which exhibit a very low polarization and a good reproducibility of the electrochemical performance in contact with LSGM solid electrolyte (Fig. 2). At 873 K, the electrode overpotential (η) was as low as −145 mV at a current density (i) of −200 mA cm^{-2}. The polarization resistance, which can be evaluated from the impedance spectra normalized to the electrode area, was lower than 1 Ohm cm^2 at 873 K (Fig. 14, inset). The electrochemical activity of $YBaCo_4O_{7+\delta}$ cathodes is higher than that of $La_2Ni_{0.8}Cu_{0.2}O_{4+\delta}$ (Table 4), another promising cathode material [41]. For instance, at 873 K and $i = 50$ mA cm^{-2}, the overpotential of cobaltite electrodes is approximately 4.5 times lower than that of nickelate layers. Most likely, the superior electrochemical activity of $YBaCo_4O_7$-based cathodes is due to their interaction with the LSGM surface, particularly Ba and Co diffusion into the surface

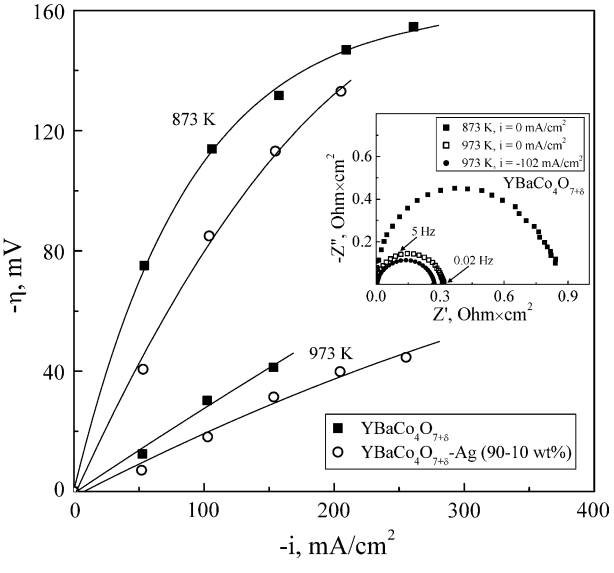

Fig. 14 Current dependencies of the cathodic overpotentials of the $YBaCo_4O_{7+\delta}$ layer with and without silver addition. The *inset* shows examples of the impedance spectra, corrected for ohmic contribution and normalized to the electrode area

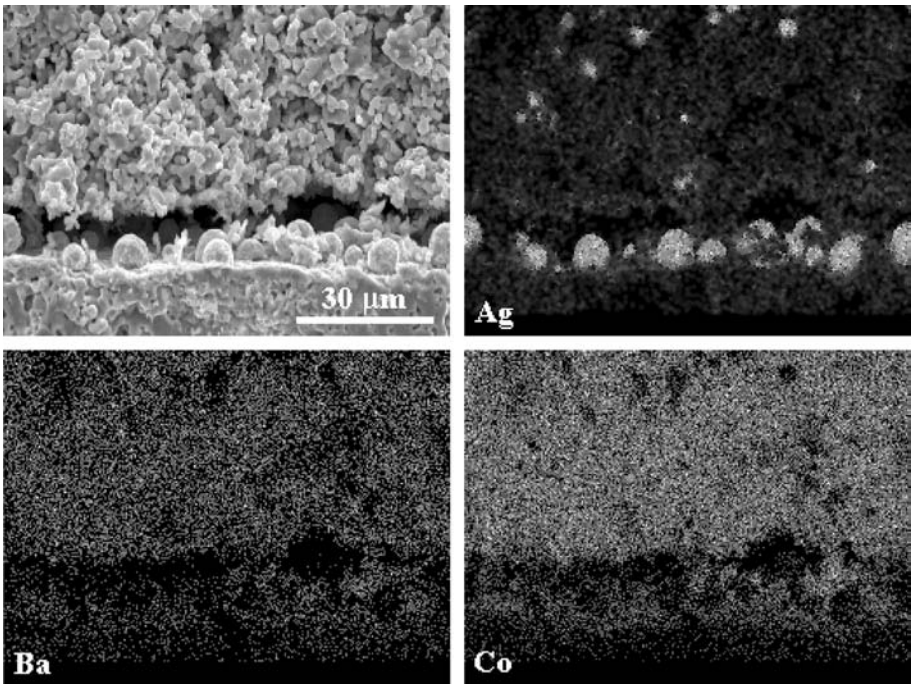

Fig. 15 SEM micrograph of fractured the $YBaCo_4O_{7+\delta}$–Ag/LSGM cell and the corresponding distribution of *Ag*, *Ba* and *Co*, evaluated by energy-dispersive spectroscopy. The density of the *white dots* corresponds to cation concentration

layer of lanthanum gallate ceramics, confirmed by the EDS studies (Fig. 15). The incorporation of cobalt into LSGM should increase both ionic and electronic conductivities of the solid electrolyte surface, thus promoting surface exchange; an increase in the oxygen exchange rates can also be expected owing to Ba diffusion (Refs. [42, 43] and references cited therein). Recently, very good electrochemical activity in contact with Co-substituted LSGM was reported for $Ba(La)CoO_{3-\delta}$ perovskite cathodes [42], the TECs of which, however, may be excessively high [3]. The excellent performance of $YBaCo_4O_{7+\delta}$ and $Ba(La)CoO_{3-\delta}$ electrodes should have a similar nature, probably owing to enhanced oxygen exchange currents of the electrolyte.

Further decrease in the cathodic overpotentials at 873–973 K can be achieved by adding metallic silver (Fig. 14, Table 4). Since the melting point of Ag (1234 K) is lower than the cell fabrication temperature, a significant amount of silver is volatilized in the course of cathode sintering at 1273 K. According to TGA, these losses correspond to 8–10 wt% of the total amount of metallic Ag. The SEM/EDS inspections showed that the remaining silver spreads mainly along the electrolyte surface, thus enhancing the triple-phase boundary; small amounts of Ag are also present in the electrode bulk (Fig. 15). Similar behavior was observed earlier for Ag-containing $La_{0.5}Sr_{0.4}MnO_3$ cathodes [18]. Nevertheless, taking into account the volume fractions of components, the porous layer of $YBaCo_4O_{7+\delta}$ should still play a dominant role in the electrochemical processes.

In summary, $YBaCo_4O_{7+\delta}$ possesses low thermal expansion, a substantial level of mixed p-type electronic and oxygen-ionic conductivity, and superior electrode properties in contact with LSGM. This phase may thus be considered for high-temperature electrochemical applications. Possible drawbacks include, however, the phase transitions under oxidizing conditions, which may limit compatibility with other materials of the electrochemical cells, and also interaction with CO_2 and water vapor in the intermediate temperature range. For membrane applications, the moderate level of oxygen permeation enables mainly thick-film approaches when the dense membrane film is deposited onto a porous substrate. In this case, mechanical stresses due to volume variations under operation conditions play a critical role. This makes further doping of $YBaCo_4O_{7+\delta}$ necessary in order to suppress phase changes and to increase stability.

Conclusions

Dense ceramics of yttrium–barium cobaltite, $YBaCo_4O_{7+\delta}$, was prepared by the standard solid-state syn-

Table 4 Overpotentials (mV) of $YBaCo_4O_{7+\delta}$ and $LaNi_{0.8}Cu_{0.2}O_{4+\delta}$ porous cathode layers in contact with LSGM electrolyte

Temperature (K)	Current density (mA cm^{-2})	$YBaCo_4O_{7+\delta}$	$YBaCo_4O_{7+\delta}$–Ag (90–10 wt%)	$LaNi_{0.8}Cu_{0.2}O_{4+\delta}$ [41]
1073	150	6.9	–	42.1
973	100	28.4	17.6	157
873	60	79.5	46.6	350

thesis route and using the GNP. No essential effect of the synthesis method on transport properties and thermal expansion was found. Within the phase stability limits, the total conductivity of $YBaCo_4O_{7+\delta}$ is predominantly p-type electronic. The ion transference numbers vary in the range 3×10^{-5}–2×10^{-4} at 1073–1223 K, and increase with temperature. The oxygen permeability of $YBaCo_4O_{7+\delta}$ ceramics, predominantly determined by the bulk ionic transport, is similar to that of K_2NiF_4-type cuprates. Heating above 1050–1100 K in air and/or redox processes under oxidizing conditions result in a slow phase transition accompanied by extensive oxygen losses from the lattice. Except for the variations associated with this transformation, the p-type electronic conductivity and the Seebeck coefficient are essentially $p(O_2)$-independent. Porous $YBaCo_4O_{7+\delta}$ electrodes, deposited onto a $LaGaO_3$-based solid electrolyte with and without addition of silver, exhibit very high electrochemical activity at 873–1073 K. In combination with moderate TECs, $(7.3–7.6)\times10^{-6}$ K^{-1} at 600–1100 K in air, this may be advantageous for practical applications if appropriate compositional modification to suppress phase changes is provided.

Acknowledgements This research was partially supported by the FCT, Portugal (project BD/6827/2001 and POCTI program), the NATO Science for Peace program (project 978002), the Spanish research program MCyT (MAT 2001-3334), the Canary Islands Government (COFI 2002/027), and the CRUP, Portugal (grant E-49/02).

References

1. Bouwmeester HJM, Burgraaf AJ (1996) Dense ceramic membranes for oxygen separation. In: Burgraaf AJ, Cot L (eds) Fundamentals of inorganic membrane science and technology. Elsevier, Amsterdam Lausanne NewYork Oxford Shannon Tokyo, pp 435–528
2. Mazanec TJ (1994) Solid State Ionics 70/71:11
3. Kharton VV, Yaremchenko AA, Naumovich EN (1999) J Solid State Electrochem 3:303
4. Pei S, Kleefisch MS, Kobylinski TP, Faber J, Udovich CA, Zhang-McCoy V, Dabrowski B, Balachandran U, Mieville RL, Poeppel RB (1995) Catal Lett 30:201
5. Kharton VV, Yaremchenko AA, Patrakeev MV, Naumovich EN, Marques FMB (2003) J Europ Ceram Soc 23:1417
6. Huang K, Lee HY, Goodenough JB (1998) J Electrochem Soc 145:3220
7. Alcock CB, Doshi RC, Shen Y (1992) Solid State Ionics 51:281
8. Vashook VV (2000) DSc Thesis, Institute of General and Inorganic Chemistry NASB, Minsk, Belarus
9. Valldor M, Andersson M (2002) Solid State Sci 4:923
10. Sheptyakov DV, Podlesnyak A, Barilo SN, Shiryaev SV, Khalyavin DD, Chernyshov DYu, Leonyuk NI (2001) PSI Sci Rep 3:64
11. Mueller-Buschbaum Hk, Rabbow C (1996) Z Naturforsch B 51:343
12. Sfreddo O, Mueller-Buschbaum Hk (1998) Z Naturforsch B 53:517
13. Brinkman HW, Kruidhof H, Burgraaf AJ (1994) Solid State Ionics 68:173
14. Kharton VV, Naumovich EN, Zhuk PP, Demin AK, Nikolaev AV (1992) Russ J Electrochem 28:1376
15. Kharton VV, Tikhonovich VN, Shuangbao Li, Naumovich EN, Kovalevsky AV, Viskup AP, Bashmakov IA, Yaremchenko AA (1998) J Electrochem Soc 145:1363
16. Kharton VV, Naumovich EN, Kovalevsky AV, Viskup AP, Figueiredo FM, Bashmakov IA, Marques FMB (2000) Solid State Ionics 138:135
17. Kharton VV, Kovalevsky AV, Yaremchenko AA, Figueiredo FM, Naumovich EN, Shaulo AL, Marques FMB (2002) J Membrane Sci 195:277
18. Tikhonovich VN, Kharton VV, Naumovich EN, Savitsky AA (1998) Solid State Ionics 106:197
19. Kharton VV, Shaula AL, Vyshatko NP, Marques FMB (2003) Electrochim Acta 48:1817
20. Chick LA, Pederson LR, Maupin GD, Bates JL, Thomas LE, Exarhos GJ (1990) Mater Lett 10:6
21. Patrakeev MV, Mitberg EB, Lakhtin AA, Leonidov IA, Kozhevnikov VL, Kharton VV, Avdeev M, Marques FMB (2002) J Solid State Chem 167:203
22. Rodriguez-Carvajal J (1993) Physica B 192:55
23. Figueiredo FM, Frade J, Marques FMB (1999) Bol Soc Esp Ceram Vidrio 38:639
24. Vogt T, Woodward PM, Karen P, Hunter BA, Henning P, Moodenbaugh AR (2000) Phys Rev Lett 84:2969
25. Fauth F, Suard E, Caignaert V, Domengés B, Mirebeau I, Keller L (2001) Eur Phys J B21:163
26. Hashimoto T, Inagaki Y, Kishi A, Dokiya M (1994) Solid State Ionics 128:227
27. Feng M, Goodenough JB (1994) Solid State Ionics 68:269
28. Anderson HU (1992) Solid State Ionics 52:33
29. Tsipis EV, Patrakeev MV, Kharton VV, Vyshatko NP, Frade JR (2002) J Mater Chem 12:3738
30. Tretiakov YuD (1974) Chemistry of nonstoichiometric oxides. Moscow State University, Moscow
31. Petrov AN, Cherepanov VA, Zuev AYu (1987) Zh Fiz Khim 61:630
32. Kharton VV, Kovalevsky AV, Viskup AP, Shaula AL, Figueiredo FM, Naumovich EN, Marques FMB (2003) Solid State Ionics 160:247
33. Kharton VV, Naumovich EN, Nikolaev AV (1994) Solid State Phenom 39–40:147
34. Kharton VV, Nikolaev AV, Naumovich EN, Samokhval VV (1994) Inorg Mater 30:492
35. Takeda Y, Kanno R, Takada T, Yamamoto O, Takano M, Bando Y (1986) Z Anorg Allg Chem 540–541:259
36. Harrison WTA, Hegwood SL, Jacobson AJ (1995) J Chem Soc Chem Commun 1953
37. Lane JA, Benson SJ, Waller D, Kilner JA (1999) Solid State Ionics 121:201
38. Avdeev MYu, Patrakeev MV, Kharton VV, Frade JR (2002) J Solid State Electrochem 6:217
39. Kharton VV, Marozau IP, Vyshatko NP, Shaula AL, Viskup AP, Naumovich EN, Marques FMB (2003) Mater Res Bull 38:773
40. Kharton VV, Viskup AP, Kovalevsky AV, Naumovich EN, Marques FMB (2001) Solid State Ionics 143:337
41. Kharton VV, Tsipis EV, Yaremchenko AA, Frade JR (2004) Solid State Ionics 166:327
42. Ishihara T, Fukui S, Nishiguchi H, Takita Y (2002) Solid State Ionics 152–153:609
43. Yamaji K, Horita T, Sakai N, Yokokawa H (2002) Solid State Ionics 152–153:517